mater.scichina.com link.springer.com

Published online 23 September 2022 | https://doi.org/10.1007/s40843-022-2181-4
Sci China Mater 2023, 66(2): 740–747

Ternary AGa_5S_8 (A = K, Rb, Cs): Promising infrared nonlinear optical materials rationally realized by "one-for-multiple substitution" strategy

Wen-Fa Chen[1,2], Xiao-Ming Jiang[1], Shao-Min Pei[1,2], Ming-Shu Zhang[1,2], Bin-Wen Liu[1*] and Guo-Cong Guo[1*]

ABSTRACT **Commercially available infrared (IR) nonlinear optical (NLO) materials, such as diamond-like $AgGaQ_2$ (Q = S, Se), display large NLO coefficients but relatively low laser-induced damage thresholds (LIDTs), which seriously hinder their widespread laser applications. Herein, the "one-for-multiple substitution" strategy, namely, [SZn_4^{6+} + $5Zn^{2+}$ ⇒ A^+ + $5Ga^{3+}$] (A = K, Rb and Cs), is applied on the diamond-like zinc-blende ZnS, and affords three new polar ternary crystals AGa_5S_8 (A = K, Rb and Cs) through the solid-state method. These compounds inherit the diamond-like anionic backbone framework in ZnS where the NLO functional motifs GaS_4 are arranged in a parallel manner. This characteristic accounts for the remarkable phase-matchable second-harmonic generation intensities (1.1–1.2 × $AgGaS_2$). In addition, the inclusion of the highly electropositive A^+ cations affords a band gap ranging from 3.10 to 3.37 eV, which facilitates the improvement of LIDT (9.3–12.4 × $AgGaS_2$). To the best our knowledge, crystals AGa_5S_8 (A = K, Rb and Cs) are the first series of ternary A-inclusion chalcogenides with large second-harmonic generation responses (≥1.0 × $AgGaS_2$) and wide band gaps (≥3.0 eV), fulfilling the rigorous requirements of outstanding IR NLO materials. In addition, the "one-for-multiple substitution" strategy presents the great significance of diamond-like structure evolution and provides a remarkable opportunity to achieve NLO materials.**

Keywords: chalcogenides, nonlinear optical materials, diamond-like structure, substitution strategy, second-harmonic generation

INTRODUCTION

The nonlinear optical (NLO) crystal is indispensable for the production of coherent and tuneable wavelengths in the all-solid-state laser technology based on optical parametric amplification or oscillation [1–18]. Typical infrared (IR) NLO materials, such as diamond-like $AgGaS_2$ (AGS), $AgGaSe_2$ and $ZnGeP_2$ [19], display large NLO intensities and wide transparent regions. However, they suffer from inherent drawbacks, like low laser-induced damage threshold (LIDT), non-phase matchable behavior, or harmful multi-phonon absorption, which limit their applications in high-power lasers. Therefore, exploring new IR NLO materials with excellent performance is still imperative in cutting-edge science and technology.

Chemical substitution based on the famous structural prototype, including mono-substitution and co-substitution, offers an alternative but effective pathway to design prominent IR NLO materials. Mono-substitution is the equivalence substitution involving one crystallographic position in the parent structure. For example, the IR NLO material $NaAsSe_2$ was synthesized from $NaAsS_2$ by this method [20,21]. Co-substitution means the replacement of two or more crystallographic positions, without the requirement of the oxidation state of each component to be equal. For instance, salt-inclusion chalcogenides $[Ba_4Cl_2]$-$[ZnGa_4S_{10}]$ were obtained by replacing K^+ and Ga^{3+} cations in $[KBa_3Cl_2][Ga_5S_{10}]$, respectively, by Ba^{2+} and Zn^+ cations in the manner of [K^+ + Ga^{3+} ⇒ Ba^{2+} + Zn^{2+}] [22,23]. To maintain the structural framework of the prototype phase, the interchangeable cations or anions should have similar sizes, which limits the selection of elements and restricts the scope of exploration. If co-substitution could be expanded to one crystallographic position substitution of multiple building units, namely, the "one-for-multiple substitution" technique, new state-of-the-art NLO materials can be further discovered.

Diamond-like chalcogenides, as the most significant family of potential IR NLO crystals, have been developed by the mono-substitution or co-substitution strategy because of the high structural flexibility of tetrahedral $[MS_4]$ (M may be Cu, Ag, Zn, Cd, Si, or Ge) units. They can originate from the zinc-blende α-ZnS in several manners, including [$2Zn^{2+}$ ⇒ I^+ + III^{3+}], [$4Zn^{2+}$ ⇒ $2I^+$ + II^{2+} + IV^{4+}], and [$7Zn^{2+}$ ⇒ $4I^+$ + II^{2+} + $2IV^{4+}$] (I = Cu, Ag, Li; II = Zn, Cd, Hg, Mn; IV = Si, Ge, Sn) [2,24–28]. Importantly, to address the low LIDT issue of the diamond-like chalcogenide AGS, a strong electropositive Li^+ substituted the photo-sensitive Ag^+ cations to obtain $LiGaS_2$ with a wide band gap and high LIDT [29]. However, Li element is corrosive to quartz tubes at high temperatures and hampers the growth of bulk crystals. Although other electropositive A^+ (A = K, Rb, Cs) cations have the same valence state to Li^+, simple substitution of A^+ with Li^+ in $LiGaS_2$ is impossible due to their substantially different ionic radii and coordination geometries. Therefore, careful molecular engineering is necessary to incorporate A^+ cations in diamond-like frameworks.

Structurally, each A atom may coordinate to 12 S atoms to form a $[AS_{12}]$ cuboctahedron, in which iso-coordinated configuration matches well with the S-centred-$[SZn_4]S_{12}$ cuboctahedron in α-ZnS. Based on the above considerations, three new ternary polar chalcogenides AGa_5S_8 (A = K, **1**; Rb, **2**; Cs, **3**) were successfully prepared by the "one-for-multiple substitution"

[1] State Key Laboratory of Structural Chemistry, Fujian Institute of Research on the Structure of Matter, Chinese Academy of Sciences, Fuzhou 350002, China
[2] University of Chinese Academy of Sciences, Beijing 100049, China
* Corresponding authors (emails: gcguo@fjirsm.ac.cn (Guo GC); bwliu@fjirsm.ac.cn (Liu BW))

strategy in the manner of $[SZn_4^{6+} + 5Zn^{2+} \Rightarrow A^+ + 5Ga^{3+}]$, that is, one tetrahedral $[SZn_4]^{6+}$ unit and five Zn^{2+} cations were replaced with one A^+ and five Ga^{3+} cations, respectively. Compounds **1**–**3** featured diamond-like anionic frameworks and produced remarkable second-harmonic generation (SHG) responses. In addition, the inclusion of the highly electropositive A^+ cation broadens the band gap and finally improves the LIDT. The three compounds represent the first series of ternary A-inclusion chalcogenides with large SHG responses (≥1.0 × AGS) and wide band gaps (≥3.0 eV). Herein, the synthesis, crystal structures, linear and NLO properties, as well as theoretical electron transition of **1**–**3** will be reported.

EXPERIMENTAL SECTION

Syntheses

All reactants were weighed in an argon-filled glovebox with O_2 levels <0.5 ppm. For the synthesis of **1**, starting materials, K metal (Sinopharm, 99%, 0.030 g), Ga metal (Alfa, 99.99%, 0.271 g), and S powder (Sinopharm, 99.9%, 0.199 g) were mixed. To synthesize **2** and **3**, raw reactants Y (Macklin, 99.99%, 0.030 g), Ga (Alfa, 99.99%, 0.117 g), S (Sinopharm, 99.9%, 0.086 g), and RbBr (0.167 g, for **2**), as well as Y (Macklin, 99.99%, 0.029 g), Ga (Alfa, 99.99%, 0.115 g), S (Sinopharm, 99.9%, 0.085 g), and CsI (0.171 g, for **3**) were mixed together. All the raw materials were placed into quartz tubes and sealed in a vacuum of 10^{-4} Torr (1 Torr = 133.3 Pa), then put in a computer-controlled furnace. They were then slowly heated to 1193 K in 25 h, kept at 1193 K for 96 h, and finally cooled to room temperature at a rate of 3 K h^{-1}. Colorless bulk crystals of **1**, **2**, and **3** were obtained by washing the products with distilled water. Energy-dispersive X-ray spectroscopy (EDS) analyses were carried out on the surfaces of single crystals using a Hitachi S-3500 scanning electron spectrometer equipped with an EDS. The EDS analyses present average A/Ga/S molar ratios near the stoichiometric ratios in **1**, **2** and **3**, respectively (Fig. S1).

Single-crystal and powder X-ray diffraction analyses

The single crystal X-ray diffraction (XRD) datasets of **1**–**3** were collected using Mo-Kα radiation (λ = 0.71073 Å) generated with a Rigaku FR-X Microfocus diffractometer at room temperature. Data collection and reduction were performed applying the CrysAlisPro [30] software, and absorption corrections were obtained based on a multiscan-type model. The crystal structures were solved by direct methods and refined on F^2 by full-matrix least-squares methods using the fifth version of Siemens SHELXTL crystallography software package [31]. For **2** and **3**, the R_1 ($I > 2\sigma(I)$) value reaches 0.0274–0.0329 when the orthorhombic system was selected, but it is larger than 0.2 when the tetragonal crystal system was applied. Thus, compounds **2** and **3** crystalize in the orthorhombic system instead of the tetragonal crystal system. All atoms were refined with anisotropic displacement parameters. The absolute structures were checked over for lacking symmetry elements using PLATON, and none were found. Powder XRD analyses were performed utilizing an automatic Rigaku Flex600 X-ray diffractometer applying Cu Kα (λ = 1.54057 Å) radiation at room temperature, with a step size of 0.02° and a 2θ range of 5°–65°.

IR and UV-Vis-NIR diffuse-reflectance spectroscopy

The IR spectra were measured by employing a Fourier transform IR spectrometer in the range of 4000–400 cm^{-1}. The ultraviolet-visible-near infrared (UV-Vis-NIR) diffuse-reflectance spectra were measured using the powder samples of **1**–**3** by a Perkin-Elmer Lambda 950 UV/Vis/NIR spectrophotometer in the wavelength range of 200–2500 nm with a $BaSO_4$ plate as a 100% reference at room temperature. The Kubelka-Munk equation was used to calculate the absorption spectra from the reflection spectra [32].

SHG and LIDT measurements

Powder SHG signals of **1**–**3** were measured by applying the Kurtz-Perry method with a laser at the wavelength of 1910 nm. Since the SHG efficiency depends on particle size, crystals of **1**–**3** were ground and sieved into several particle sizes (30–50, 50–75, 75–100, 100–150, and 150–200 μm), which were placed between the glass plates. The commercial AGS samples as standards were sieved into the same particle size ranges. The LIDT was measured using crystals **1**–**3** and AGS with the laser source (1064 nm, 10 ns, 1 Hz). The laser emission's energy was gradually increased until the damage to samples occurred. The damage threshold is defined as $I_{(\text{threshold})} = E/(\pi r^2 t_p)$, where E, r, and t_p refer to the energy of a single pulse, spot radius, and pulse width, respectively.

Calculations of electronic structures and optical properties

First-principles calculations on compounds **1**–**3** were performed using the ABINIT software package, a total energy package based on the pseudopotential density functional theory (DFT) [33–36]. The correlation-exchange terms in the Hamiltonian were described by the functional developed by Perdew, Burke, and Ernzerhof in the generalized gradient approximation form. The projector-augmented plane-wave pseudopotentials (K $3s^23p^64s^1$, Rb $4s^24p^65s^1$, Cs $5s^25p^66s^1$, Ga $3d^{10}4s^24p^1$, and S $3s^23p^4$) were used to simulate ion-electron interactions for all constituent elements. A kinetic energy cutoff of 18 Hartree was chosen with Monk Horst-Pack k-point meshes (4 × 3 × 2 for **1**, and 2 × 2 × 2 for **2** and **3**, respectively) in the Brillouin zone. For calculating the linear optical properties, the dielectric function is defined as $\varepsilon_{ij} = \varepsilon_{ij,\text{re}}(\omega) + \varepsilon_{ij,\text{im}}(\omega)$ utilizing $\frac{4\pi}{\Omega}\sum_{\text{nmk}} f_{\text{nm}}(k)\frac{r^i_{\text{nm}}(k) r^j_{\text{mn}}(k)}{\omega_{\text{mn}}(k) - \omega} + \delta_{ij}$, in which $\varepsilon_{\text{re}}(\omega)$ are real parts of the dielectric function, $\varepsilon_{\text{im}}(\omega)$ are imaginary parts of the dielectric function, and $r^i_{\text{nm}}(k)$ is the position matrix elements from states n to m. The density functional perturbation theory and the "sum over states" method were used to calculate the frequency-dependent SHG susceptibility tensor $\chi_{ijk}(2\omega,\omega,\omega)$. The SHG susceptibility primarily stems from three parts: (1) the pure inter-band transition term $\chi_{\text{inter}}(2\omega,\omega,\omega)$; (2) the intra-band transition term $\chi_{\text{intra}}(2\omega,\omega,\omega)$, which describes the modulation of linear susceptibility by the intra-band motion of electron; and (3) the modulation term $\chi_{\text{mod}}(2\omega,\omega,\omega)$ of the intra-band contribution by the inter-band motion-related polarization energy [35].

RESULTS AND DISCUSSION

Crystal structures

Single crystals of **1**–**3** were synthesised with high yield *via* the solid-state method in sealed quartz tubes. The purities of phases **1**–**3** were verified by powder XRD (Fig. S2). As listed in Table 1,

Table 1 Crystal data and structure refinement parameters for **1**–**3**

Empirical formula	KGa_5S_8 (**1**)	$RbGa_5S_8$ (**2**)	$CsGa_5S_8$ (**3**)
Formula weight	644.18	690.55	738.00
Temperature (K)		293(2)	
Space group	$P2_1$	*Iba*2	*Iba*2
a (Å)	8.3639(4)	22.3100(5)	22.3837(5)
b (Å)	10.1146(4)	22.3100(5)	22.3837(5)
c (Å)	15.2948(7)	10.3387(3)	10.3799(5)
β (°)	101.877(4)	90	90
V (Å^3)	1266.2(1)	5145.9(2)	5200.6(3)
Z	4	2	2
D_{calc} (g cm^{-3})	3.379	3.565	3.770
μ (mm^{-1})	12.101	15.346	14.225
Goodness-of-fit on F^2	0.990	0.994	1.002
R_1[a] ($I > 2(I)$)	0.0267	0.0329	0.0274
wR_2[b] ($I > 2(I)$)	0.0562	0.0773	0.0548
R_1[a] (all data)	0.0336	0.0364	0.0345
wR_2[b] (all data)	0.0588	0.0784	0.0571
Flack x	0.022(14)	−0.001(10)	0.01(3)
$\Delta\rho_{max}/\Delta\rho_{min}$, (e Å^{-3})	0.744/−0.645	0.911/−1.099	0.661/−0.552

a) $R_1 = \Sigma||F_o|-|F_c||/\Sigma|F_o|$, b) $wR_2 = (\Sigma(w(F_o^2-F_c^2)^2)/\Sigma(w(F_o^2)^2))^{1/2}$.

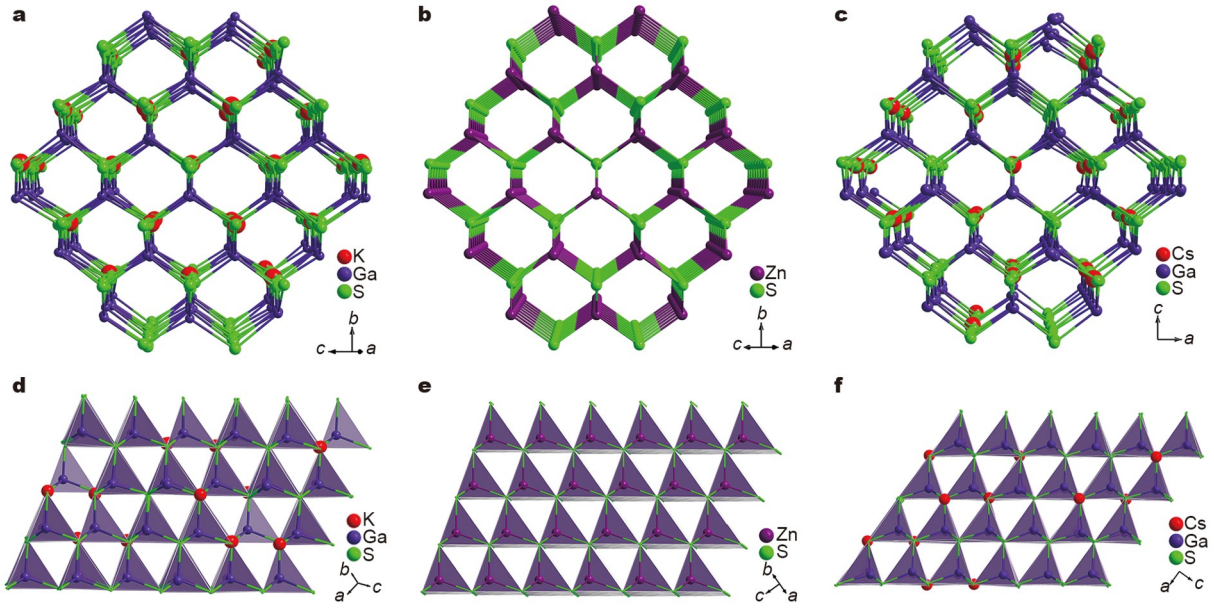

Figure 1 Open honeycomb-like structures of **1** (a), α-ZnS (b) and **3** (c). The tetrahedral GaS_4 (or ZnS_4) units were highly arranged in **1** (d), α-ZnS (e) and **3** (f).

single-crystal XRD studies demonstrate that **1** crystallizes in the monoclinic space $P2_1$ and the asymmetric units of **1**–**3** consist of two A sites, 10 Ga sites, and 16 S independent sites (Table S1). All Ga atoms connect four S atoms to form slight GaS_4 tetrahedrons with Ga–S bond distances of 2.205–2.385 Å (Table S2), which almost coincides with those of $BaGa_2GeS_6$ [37], Sm_4GaSbS_9 [38], $Ba_6Zn_7Ga_2S_{16}$ [39], and $LiGa_2PS_6$ [40]. All GaS_4 tetrahedrons are anchored *via* corner-sharing S atoms to produce three-dimensional diamond-like anionic frameworks, in which A^+ cations are located in the cavities to keep the electrovalence balanced. According to the calculation method in the literature [41], the densities of the [GaS_4] group (n/V) of compounds **1**, **2**, and **3** are 0.0158, 0.0142, and 0.0140 Å^{-3}, respectively. Compounds **1**–**3** show similar honeycomb-like frameworks resembling that of α-ZnS (Fig. 1) [42], which belong to the structural progenitor for diamond-like metal chalcogenides. The compounds can be described as large-size A^+ cations located in the diamond-like anionic frameworks.

Elucidating the structural evolution from α-ZnS (sphalerite) to the title compounds is significant. On the one hand, each ion in

the binary α-ZnS is tetrahedrally coordinated by the nearest neighbor cations, in which the $[SZn_4]$ tetrahedron is surrounded by 12 S atoms to build a tetrakaidecahedron with bond distances of S(centre)–S(terminal) ranging over 3.8 Å. The valence-balanced A^+ cations are also bonded to 12 S atoms to build a tetrakaidecahedron (Fig. 2) with distance lengths of K/Rb/Cs–S ranging from 3.5 to 3.9 Å, which are coordination-matched with $[SZn_4]S_{12}$ units. On the other hand, the tetrahedral $[ZnS_4]$ and $[GaS_4]$ units are known to exhibit similar coordinated configurations and can substitute each other. Given that the substitution should maintain the sum of the oxidation states constant, the "one-for-multiple substitution" strategy from the maternal structures to the derivatives is performed; that is, $[SZn_4^{6+} + 5Zn^{2+} \Rightarrow A^+ + 5Ga^{3+}]$, in which the $[SZn_4]^{6+}$ units and $5Zn^{2+}$ cations are replaced with A^+ and $5Ga^{3+}$ cations, respectively, resulting in the synthesis of the title compounds.

Interestingly, despite the same stoichiometric ratio, phases **1**–**3** adopt different space groups owing to the cation size effect. Numerous known compounds exhibit similar phenomena. For instance, the decrease of structural symmetries was discovered in the $A_2Hg_3Ge_2S_8$ (A = alkali metal) [43–45] system with distinct A element replacements. Also, different A atoms in the SrA_2SiS_4 (A = Li, Na, Cu) [46] series caused them to represent distinct coordination numbers and dimensional configurations. Notably, the Rb^+ and Cs^+ (corresponding ionic radii of 1.72 and 1.88 Å) cations are relatively larger than K^+ (ionic radius: 1.64 Å) in title compounds, leading to K/Rb/Cs–S average distance lengths of 3.64, 3.66 and 3.68 Å (Table S2), respectively, accounting for the change in the interactions between the cation and anionic framework. Such slight changes in the bond length directly affected the rising crystallographic symmetry from the mono-clinic space $P2_1$ to the orthorhombic space *Iba*2 but not greatly influenced the similar diamond-like anionic frameworks with the tetrahedrons alignment in parallel fashions. This phase-change attribute offered great significance to the diamond-like structural evolution.

SHG and LIDT

Given that all tetrahedrons in the diamond-like anionic frameworks were highly oriented arrays, **1**–**3** may disclose large NLO coefficients. The SHG responses of the compounds and standard AGS were measured by the Kurtz and Perry powder technique [47] under laser radiation at 1910 nm. The relative SHG intensities of **1**–**3** increased and nearly reached platforms dependent on particle sizes, indicating phase matchable attributes. When the particle size reached the range of 150–200 μm, the corresponding SHG intensities of **1**, **2** and **3** were 1.2, 1.1 and 1.2 times that of the benchmark AGS (Fig. 3a and Fig. S3). Therefore, the corresponding SHG coefficients d_{eff} of **1**, **2** and **3** were calculated to be 12.7, 12.2 and 12.7 pm V^{-1} with the benchmark AGS (d_{eff} = 11.6 pm V^{-1}, $d_{eff(sample)}/d_{eff(AGS)} = (I_{2\omega(sample)}/I_{2\omega(AGS)})^{1/2}$) [23]. Such data were larger than those of new IR NLO crystals, such as $AAgGa_6S_{10}$ (A = K, Rb, Cs) [48], $Li_4MgGe_2S_7$ [2], $[K_4Cl][CdGa_9S_{16}]$ [49], and $[ABa_2Cl][Ga_4S_8]$ (A = Rb, Cs) [50].

The LIDT is a significant parameter for evaluating the NLO crystal to be applied in a high-power laser. As shown in Fig. 3b and Table S3, the corresponding LIDT values of **1** (crystal size: 2.1 mm × 2.0 mm × 1.5 mm), **2** (1.5 mm × 1.2 mm × 0.5 mm) and **3** (2.0 mm × 1.1 mm × 1.0 mm) (see the inset of Fig. 3c) were measured to be 134.8, 109.9 and 101.0 MW cm^{-2}, which were 12.4, 10.1 and 9.3 times that of AGS (10.9 MW cm^{-2}, 2.0 mm × 1.5 mm × 1.0 mm) as shown by the single-pulse method at the fundamental laser of 1064 nm [51]. Thus, the LIDT values of **1**–**3** were close to those of notable $BaGa_4S_7$ [52] and $Li[Cs_2LiCl][Ga_3S_6]$ [53]. In general, the band gap of chalcogenides is positively related to the LIDT [54]. The UV-Vis-NIR diffuse reflectance spectra in Fig. 3c showed strong absorption edges at 3.23, 3.10 and 3.37 eV for **1**, **2** and **3**, respectively. By comparison, the A^+ substitutions with Ag^+ cations in AGS broadened their band gaps [55]. Because compounds **1**–**3** could mitigate the multiple-photon absorption under the 1064-nm laser irradiation, they are subsequently beneficial for the improved LIDTs. Moreover, thermal properties are also crucial factors that influence the LIDT. The temperature-dependent lattice parameters of **1**–**3** were studied at temperatures ranging from 100 to 300 K. The thermal expansion coefficients (at × 10^{-5}; Fig. 3d and Fig. S4) were as follows: 1.36, 0.82 and 0.98 for **1**; 1.26 and 1.06 for **2**; and 1.43 and 1.15 for **3**. Thus, the corresponding thermal expansion anisotropies (Table S4) of **1**, **2** and **3** were 0.66, 0.19 and 0.24, which were considerably smaller than those of AGS (2.95) [23]. These values indicated the high LIDTs of **1**–**3**.

Traditionally, ternary systems usually have simple chemical compositions and convenient syntheses, which are superior to the quaternary (or pentanary) ones for practical applications. Following these considerations, the properties of ternary classical and title IR NLO crystals are listed in Table 2. **1**–**3** showed strong NLO coefficients (equal to that of AGS), and broadened

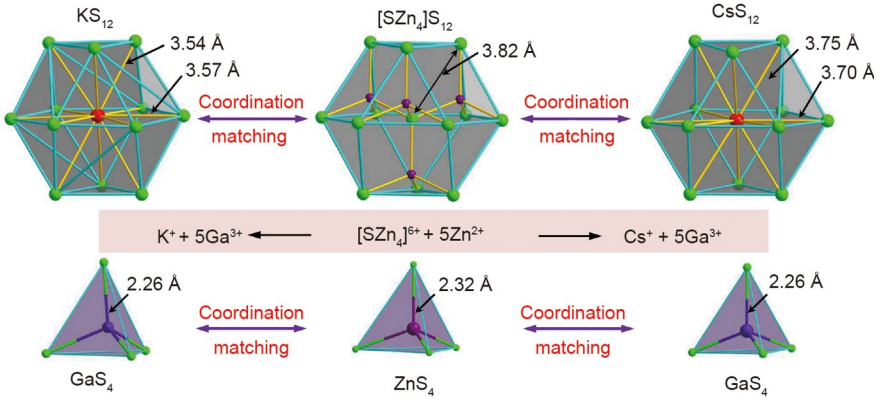

Figure 2 Structural evolution from α-ZnS to **1**–**3** realized by the co-substitution strategy.

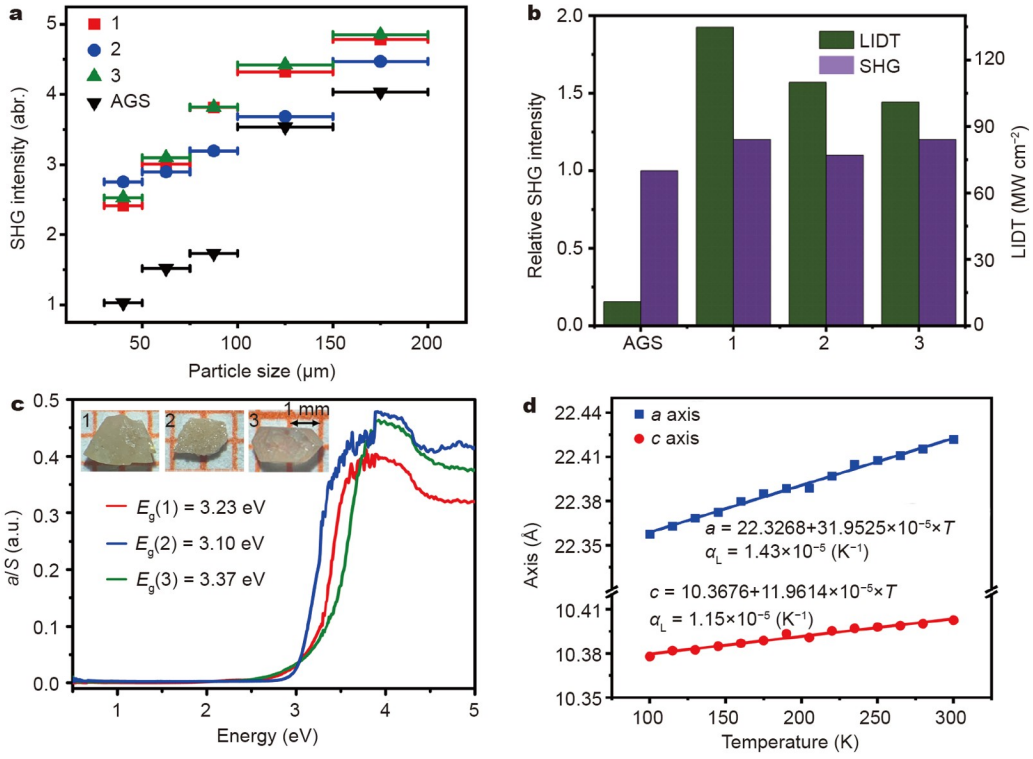

Figure 3 (a) Phase-matchable behaviours of **1**–**3** and benchmark AGS. (b) Relative SHG intensities and LIDTs. (c) Diffuse reflectance spectra of **1**–**3** (inset: the single-crystals of **1**–**3**). (d) Thermal expansion coefficients of **3**.

Table 2 Comparison of the NLO properties of ternary typical and title IR NLO sulfides

Compounds	Relative SHG[a] (×AGS)	Relative LIDT (×AGS)	Band gap (eV)	Ref.
AGS	1.0	1.0	2.65	[19]
$LiGaS_2$	0.4	8.3	4.15	[56,57]
$LiInS_2$	0.5	3.3	3.59	[56,58]
$BaGa_4S_7$	0.4	7.8	3.54	[52,56]
1	1.2	12.4	3.23	This work
2	1.1	10.1	3.10	This work
3	1.2	9.3	3.37	This work

a) The nonlinear coefficients were equal to max($|d_{ij}|$).

band gaps (larger than 3.0 eV) that were positively related to high LIDT (~10 times that of AGS) simultaneously. To the best of our knowledge, samples **1**–**3** are the first ternary A-inclusion chalcogenides with large SHG responses (≥1.0 × AGS) and wide band gaps (≥3.0 eV), which fulfill the advanced requirements, suggesting their potential for high-power applications. Furthermore, broad spectral ranges (2.5–25.0 mm) are shown by the IR transmission spectra in Fig. S5. This result indicates that **1**–**3** may be used for prominent NLO applications in the mid-IR and far-IR regions.

Electronic structure and NLO efficiency calculations

To gain further insight on the structure-property relationships, the electronic structure, density of states (DOS) and optical properties of **1**–**3** were investigated by the DFT [34–36]. As illustrated in Fig. 4a and Fig. S6, **1**, **2** and **3** had calculated indirect band gaps of 2.30, 2.22 and 2.22 eV, respectively. The partial DOSs are depicted in Fig. 4b and Fig. S6. The K (or Rb, Cs) orbitals were electropositive and located at a deep level that made a negligible contribution at both the top of valance bands and the bottom of conduction bands. This A^+ configuration played wide band gap roles due to the "dimensional reduction" effect [59]. By contrast, the electron transition was mainly completed in Ga-s, p and S-s, p orbits close to the band gap. That is, given that the optical properties primarily originated from the electron transitions, the SHG responses of **1**–**3** were mainly contributed by the tetrahedral GaS_4 units. Moreover, based on the restrictions of the Kleinman's symmetry, the independent SHG coefficient of **1** is four, but those for **2** and **3** are three. The frequency-dependent SHG coefficients of 0.65 eV (1910 nm) (Fig. 4c, d and Fig. S7) depicted that the calculated values for d_{16}, d_{14}, d_{22}, and d_{24}, were 13.0, 13.6, 3.1, and −10.5 pm V^{-1} for **1**; d_{15}, d_{24} and d_{33} were −20.5, 20.1 and −0.4 pm V^{-1} for **2**; and −18.6, 18.5, and −0.16 pm V^{-1} for **3**. The experimental ones of **1**–**3** kept in certain values between the frequency-dependent SHG coefficients.

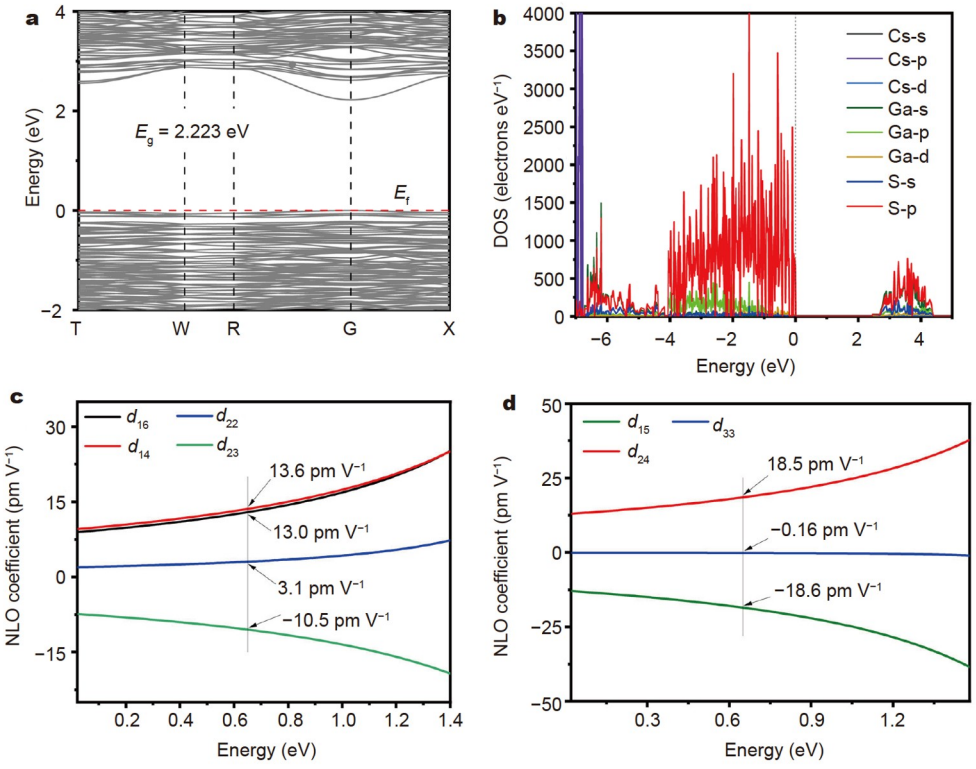

Figure 4 (a) Calculated band structure of **3**. (b) Partial DOS of **3**. Calculated NLO coefficients of **1** (c) and **3** (d).

CONCLUSIONS

In summary, the "one-for-multiple substitution" strategy was proposed and applied on zinc-blende ZnS, successfully affording ternary new chalcogenides AGa_5S_8 (A = K, Rb, Cs) in the manner of [9ZnS ⇒ SZn_4^{6+} + $5Zn^{2+}$ ⇒ A^+ + $5Ga^{3+}$]. These compounds feature diamond-like anionic frameworks, in which tetrahedral GaS_4 units are arranged in parallel fashions, leading to large phase-matching SHG responses of 1.1–1.2 times that of the benchmark $AgGaS_2$. The presence of the strongly electropositive A^+ cations increases the band gap to 3.10–3.37 eV, which facilitates the boosting of the LIDT to more than ~10-fold that of $AgGaS_2$. Thus, balanced property requirements, such as large phase-matchable NLO coefficient (≥1.0 × $AgGaS_2$), wide band gap (≥3.0 eV) and broad transmittance ranges, are fully satisfied. Compounds **1**–**3** are promising IR NLO materials, and studies on the growth of bulk single crystals are ongoing. This research provides a feasible method for designing new ternary diamond-like NLO materials with strong NLO responses and wide band gaps.

Received 26 May 2022; accepted 4 July 2022; published online 23 September 2022

1 Mutailipu M, Poeppelmeier KR, Pan S. Borates: A rich source for optical materials. Chem Rev, 2021, 121: 1130–1202
2 Abudurusuli A, Huang J, Wang P, *et al.* $Li_4MgGe_2S_7$: The first alkali and alkaline-earth diamond-like infrared nonlinear optical material with exceptional large band gap. Angew Chem Int Ed, 2021, 60: 24131–24136
3 Gao L, Huang J, Guo S, *et al.* Structure-property survey and computer-assisted screening of mid-infrared nonlinear optical chalcohalides. Coord Chem Rev, 2020, 421: 213379
4 Mutailipu M, Li F, Jin C, *et al.* Strong nonlinearity induced by coaxial alignment of polar chain and dense [BO_3] units in $CaZn_2(BO_3)_2$. Angew Chem Int Ed, 2022, 61: e202202096
5 Xia M, Li F, Mutailipu M, *et al.* Discovery of first magnesium fluorooxoborate with stable fluorine terminated framework for deep-UV nonlinear optical application. Angew Chem Int Ed, 2021, 60: 14650–14656
6 Gong P, Liang F, Kang L, *et al.* Mid-infrared nonlinear optical halides with diamond-like structures: A theoretical and experimental study. Chem Mater, 2022, 34: 5301–5310
7 Li XH, Shi ZH, Yang M, *et al.* $Sn_7Br_{10}S_2$: The first ternary halogen-rich chalcohalide exhibiting a chiral structure and pronounced nonlinear optical properties. Angew Chem Int Ed, 2022, 61: e202115871
8 Pan Y, Guo SP, Liu BW, *et al.* Second-order nonlinear optical crystals with mixed anions. Coord Chem Rev, 2018, 374: 464–496
9 Chen X, Jo H, Ok KM. Lead mixed oxyhalides satisfying all fundamental requirements for high-performance mid-infrared nonlinear optical materials. Angew Chem Int Ed, 2020, 59: 7514–7520
10 Dong X, Huang L, Zeng H, *et al.* High-performance sulfate optical materials exhibiting giant second harmonic generation and large birefringence. Angew Chem Int Ed, 2022, 61: e202116790
11 Chen J, Chen H, Xu F, *et al.* $Mg_2In_3Si_2P_7$: A quaternary diamond-like phosphide infrared nonlinear optical material derived from $ZnGeP_2$. J Am Chem Soc, 2021, 143: 10309–10316
12 Li RA, Zhou Z, Lian YK, *et al.* A_2SnS_5: A structural incommensurate modulation exhibiting strong second-harmonic generation and a high laser-induced damage threshold (A = Ba, Sr). Angew Chem Int Ed, 2020, 59: 11861–11865
13 Zhang Y, Bian Q, Wu H, *et al.* Designing a new infrared nonlinear optical material, β-$BaGa_2Se_4$ inspired by the phase transition of the BaB_2O_4 (BBO) crystal. Angew Chem Int Ed, 2022, 134: e202115374
14 Jiang XM, Deng S, Whangbo MH, *et al.* Material research from the viewpoint of functional motifs. Natl Sci Rev, 2022, 9
15 Li MY, Li B, Lin H, *et al.* $Sn_2Ga_2S_5$: A polar semiconductor with exceptional infrared nonlinear optical properties originating from the combined effect of mixed asymmetric building motifs. Chem Mater, 2019, 31: 6268–6275

16 Xing W, Tang C, Wang N, *et al.* $AXHg_3P_2S_8$ (A = Rb, Cs; X = Cl, Br): New excellent infrared nonlinear optical materials with mixed-anion chalcohalide groups of trigonal planar $[HgS_2X]^{3-}$ and tetrahedral $[HgS_3X]^{5-}$. Adv Opt Mater, 2021, 9: 2100563
17 Wu C, Jiang X, Lin L, *et al.* A congruent-melting mid-infrared nonlinear optical vanadate exhibiting strong second-harmonic generation. Angew Chem Int Ed, 2021, 60: 22447–22453
18 Chen WF, Liu BW, Pei SM, *et al.* ASb_5S_8 (A = K, Rb, and Cs): Thermal switching of infrared nonlinear optical properties across the crystal/glass transformation. Chem Mater, 2021, 33: 3729–3735
19 Nikogosyan DN. Nonlinear Optical Crystals: A Complete Survey, 1st ed. New York: Springer, 2005, 75–107
20 Bera TK, Song JH, Freeman AJ, *et al.* Soluble direct-band-gap semiconductors $LiAsS_2$ and $NaAsS_2$: Large electronic structure effects from weak As···S interactions and strong nonlinear optical response. Angew Chem Int Ed, 2008, 47: 7828–7832
21 He J, Iyer AK, Waters MJ, *et al.* Giant non-resonant infrared second order nonlinearity in γ-$NaAsSe_2$. Adv Opt Mater, 2021, 10: 2101729
22 Chen H, Li YY, Li B, *et al.* Salt-inclusion chalcogenide $[Ba_4Cl_2]$-$[ZnGa_4S_{10}]$: Rational design of an IR nonlinear optical material with superior comprehensive performance derived from $AgGaS_2$. Chem Mater, 2020, 32: 8012–8019
23 Liu BW, Zeng HY, Jiang XM, *et al.* Phase matching achieved by bandgap widening in infrared nonlinear optical materials $[ABa_3Cl_2]$-$[Ga_5S_{10}]$ (A= K, Rb, and Cs). CCS Chem, 2021, 3: 964–973
24 Liang F, Kang L, Lin Z, *et al.* Analysis and prediction of mid-IR nonlinear optical metal sulfides with diamond-like structures. Coord Chem Rev, 2017, 333: 57–70
25 Guo Y, Liang F, Li Z, *et al.* $Li_4HgSn_2Se_7$: The first second-order nonlinear optical-active selenide in the I_4–II–IV_2–VI_7 diamond-like family. Cryst Growth Des, 2019, 19: 5494–5497
26 Zhang JH, Clark DJ, Brant JA, *et al.* α-Li_2ZnGeS_4: A wide-bandgap diamond-like semiconductor with excellent balance between laser-induced damage threshold and second harmonic generation response. Chem Mater, 2020, 32: 8947–8955
27 Zhang JH, Stoyko SS, Craig AJ, *et al.* Phase matching, strong frequency doubling, and outstanding laser-induced damage threshold in the biaxial, quaternary diamond-like semiconductor $Li_4CdSn_2S_7$. Chem Mater, 2020, 32: 10045–10054
28 Li G, Chu Y, Zhou Z. From $AgGaS_2$ to Li_2ZnSiS_4: Realizing impressive high laser damage threshold together with large second-harmonic generation response. Chem Mater, 2018, 30: 602–606
29 Isaenko L, Yelisseyev A, Lobanov S, *et al.* Growth and properties of $LiGaX_2$ (X = S, Se, Te) single crystals for nonlinear optical applications in the mid-IR. Cryst Res Technol, 2003, 38: 379–387
30 Rigaku Oxford Diffraction, 2019, CrysAlisPro Software system, version v40.67a, Rigaku Corporation, Oxford, UK
31 Siemens. SHELXTL Version 5 Reference Manual. Siemens Energy &Automation Inc., Madison, WI, 1994
32 Korum G. Reflectance Spectroscopy. New York: Springer, 1969, 1–336
33 Gonze X. Perturbation expansion of variational principles at arbitrary order. Phys Rev A, 1995, 52: 1086–1095
34 Gonze X. Adiabatic density-functional perturbation theory. Phys Rev A, 1995, 52: 1096–1114
35 Baroni S, de Gironcoli S, dal Corso A, *et al.* Phonons and related crystal properties from density-functional perturbation theory. Rev Mod Phys, 2001, 73: 515–562
36 Ghosez P, Gonze X, Godby RW. Long-wavelength behavior of the exchange-correlation kernel in the Kohn-Sham theory of periodic systems. Phys Rev B, 1997, 56: 12811–12817
37 Yin W, Feng K, He R, *et al.* $BaGa_2MQ_6$ (M = Si, Ge; Q = S, Se): A new series of promising IR nonlinear optical materials. Dalton Trans, 2012, 41: 5653–5661
38 Chen MC, Li LH, Chen YB, *et al.* In-phase alignments of asymmetric building units in Ln_4GaSbS_9 (Ln = Pr, Nd, Sm, Gd–Ho) and their strong nonlinear optical responses in middle IR. J Am Chem Soc, 2011, 133: 4617–4624
39 Li YY, Liu PF, Wu LM. $Ba_6Zn_7Ga_2S_{16}$: A wide band gap sulfide with phase-matchable infrared NLO properties. Chem Mater, 2017, 29: 5259–5266
40 Feng J, Hu CL, Li B, *et al.* $LiGa_2PS_6$ and $LiCd_3PS_6$: Molecular designs of two new mid-infrared nonlinear optical materials. Chem Mater, 2018, 30: 3901–3908
41 Zou G, Ye N, Huang L, *et al.* Alkaline-alkaline earth fluoride carbonate crystals $ABCO_3F$ (A = K, Rb, Cs; B = Ca, Sr, Ba) as nonlinear optical materials. J Am Chem Soc, 2011, 133: 20001–20007
42 Jamieson JC, Demarest Jr. HH. A note on the compression of cubic ZnS. J Phys Chem Solids, 1980, 41: 963–964
43 Wu K, Yang Z, Pan S. $Na_2Hg_3M_2S_8$ (M = Si, Ge, and Sn): New infrared nonlinear optical materials with strong second harmonic generation effects and high laser-damage thresholds. Chem Mater, 2016, 28: 2795–2801
44 Liao JH, Marking GM, Hsu KF, *et al.* α- and β-$A_2Hg_3M_2S_8$ (A = K, Rb; M = Ge, Sn): Polar quaternary chalcogenides with strong nonlinear optical response. J Am Chem Soc, 2003, 125: 9484–9493
45 Marking GA, Hanko JA, Kanatzidis MG. New quaternary thiostannates and thiogermanates $A_2Hg_3M_2S_8$ (A = Cs, Rb; M = Sn, Ge) through Molten A_2S_x. Reversible glass formation in $Cs_2Hg_3M_2S_8$. Chem Mater, 1998, 10: 1191–1199
46 Yang Y, Wu K, Wu X, *et al.* A new family of quaternary thiosilicates SrA_2SiS_4 (A = Li, Na, Cu) as promising infrared nonlinear optical crystals. J Mater Chem C, 2020, 8: 1762–1767
47 Kurtz SK, Perry TT. A powder technique for the evaluation of nonlinear optical materials. J Appl Phys, 1968, 39: 3798–3813
48 Li JN, Li XH, Yao WD, *et al.* New nonlinear optical-active $AAgGa_6S_{10}$ (A = K, Rb, Cs) featuring $\{[AgGa_6S_{10}]^-\}_\infty$ framework and high laser damage threshold. Chem Commun, 2021, 57: 5175–5178
49 Pei SM, Liu BW, Jiang XM, *et al.* Superior infrared nonlinear optical performance achieved by synergetic functional motif and vacancy site modulations. Chem Mater, 2021, 33: 8831–8837
50 Liu BW, Jiang XM, Zeng HY, *et al.* $[ABa_2Cl][Ga_4S_8]$ (A = Rb, Cs): Wide-spectrum nonlinear optical materials obtained by polycation-substitution-induced nonlinear optical (NLO)-functional motif ordering. J Am Chem Soc, 2020, 142: 10641–10645
51 Zhang MJ, Jiang XM, Zhou LJ, *et al.* Two phases of Ga_2S_3: Promising infrared second-order nonlinear optical materials with very high laser induced damage thresholds. J Mater Chem C, 2013, 1: 4754–4760
52 Guo Y, Zhou Y, Lin X, *et al.* Growth and characterizations of $BaGa_4S_7$ crystal. Optical Mater, 2014, 36: 2007–2011
53 Liu BW, Jiang XM, Li BX, *et al.* $Li[LiCs_2Cl][Ga_3S_6]$: A nanoporous framework of GaS_4 tetrahedra with excellent nonlinear optical performance. Angew Chem Int Ed, 2020, 59: 4856–4859
54 Zhang G, Li Y, Jiang K, *et al.* A new mixed halide, $Cs_2HgI_2Cl_2$: Molecular engineering for a new nonlinear optical material in the infrared region. J Am Chem Soc, 2012, 134: 14818–14822
55 Bhar GC, Smith RC. Optical properties of II–IV–V2 and I–III–VI2 crystals with particular reference to transmission limits. Phys Stat Sol (a), 1972, 13: 157–168
56 Isaenko LI, Yelisseyev AP. Recent studies of nonlinear chalcogenide crystals for the mid-IR. Semicond Sci Technol, 2016, 31: 123001
57 Tyazhev A, Vedenyapin V, Marchev G, *et al.* Singly-resonant optical parametric oscillation based on the wide band-gap mid-IR nonlinear optical crystal $LiGaS_2$. Optical Mater, 2013, 35: 1612–1615
58 Fossier S, Salaün S, Mangin J, *et al.* Optical, vibrational, thermal, electrical, damage, and phase-matching properties of lithium thioindate. J Opt Soc Am B, 2004, 21: 1981–2007
59 Androulakis J, Peter SC, Li H, *et al.* Dimensional reduction: A design tool for new radiation detection materials. Adv Mater, 2011, 23: 4163–4167

Acknowledgements This work was supported by the National Natural Science Foundation of China (21827813, 21921001, 22175172, 22075283, and 92161125), the Youth Innovation Promotion Association of Chinese Academy of Sciences (2020303 and 2021300), and the Natural Science Foundation of Fujian Provinces, China (2020J01115).

Author contributions Chen WF performed the experiments, data analyses,

and paper writing; Jiang XM performed the theoretical analyses; Liu BW and Guo GC guided and supervised the experiments, and revised the paper. All authors contributed to the general discussion.

Conflict of interest The authors declare that they have no conflict of interest.

Supplementary information Supporting data are available in the online version of the paper.

Wen-Fa Chen received his BE degree from Beijing University of Chemical Technology in 2017 and ME degree in materials engineering from the University of Chinese Academy of Sciences in 2021. He is currently a PhD student and focuses on nonlinear optical materials at the University of Chinese Academy of Sciences.

Bin-Wen Liu received his BE degree from Hunan University in 2010 and PhD degree in inorganic chemistry from Fujian Institute of Research on the Structure of Matter, Chinese Academy of Sciences in 2016. Since 2019, he has been working as an associate professor at Fujian Institute of Research on the Structure of Matter. His current research interests include solid-state inorganic chemistry, and nonlinear optical materials.

Guo-Cong Guo received his BS degree from Xiamen University in 1986 and PhD degree from The Chinese University of Hong Kong in 1999. Since 2000, he has been working as a full professor at Fujian Institute of Research on the Structure of Matter, Chinese Academy of Sciences. His current research interests include inorganic-organic hybrid photofunctional materials, infrared nonlinear optical materials, and catalytic materials.

三元AGa_5S_8 (A = K, Rb, Cs): 通过“一替多取代”策略制备的红外非线性光学材料

陈文发[1,2], 姜小明[1], 裴绍敏[1,2], 张铭枢[1,2], 刘彬文[1*], 郭国聪[1*]

摘要 目前, 商用的红外非线性光学晶体材料, 如具有类金刚石结构的硫属化合物$AgGaQ_2$ (Q = S, Se), 具有强的非线性光学系数. 然而, 相对较低的抗激光损伤阈值制约了其在高能激光领域的应用. 以类金刚石结构的闪锌矿ZnS为模板, 我们通过“一替多取代”策略, 即[SZn_4^{6+} + $5Zn^{2+}$ ⇒ A^+ + $5Ga^{3+}$] (A = K、Rb和Cs), 采用固相合成方法, 获得了三元晶体AGa_5S_8 (A = K、Rb和Cs). 极性结构的AGa_5S_8保持了类金刚石阴离子骨架框架, 非线性光学功能基元GaS_4四面体以平行排列的方式堆积, 使其具有高的相位匹配倍频强度(1.1–1.2 × $AgGaS_2$); 另外, 含有高正电性A^+阳离子使其表现出3.10–3.37 eV的宽带隙, 进而提高抗激光损伤阈值(9.3–12.4 × $AgGaS_2$). 晶体AGa_5S_8 (A = K、Rb和Cs)是第一个具有大倍频响应(≥1.0 × $AgGaS_2$)和宽带隙(≥3.0 eV)的三元含碱金属的硫属化合物, 满足了优秀红外非线性光学材料的严格要求. 此外, “一替多取代”策略在类金刚石结构演变中具有重要意义, 并为获得新非线性光学材料提供了良好的机遇.

